ADVANCED FUNCTIONAL MATERIALS
www.afm-journal.de

Van der Waals $SnSe_{2(1-x)}S_{2x}$ Alloys: Composition-Dependent Bowing Coefficient and Electron–Phonon Interaction

Zakhar R. Kudrynskyi, Xueting Wang, Jake Sutcliffe, Mahabub A. Bhuiyan, Yuhao Fu, Zhuo Yang, Oleg Makarovsky, Laurence Eaves, Andrij Solomon, Volodymyr T. Maslyuk, Zakhar D. Kovalyuk, Lijun Zhang, and Amalia Patanè**

The design of advanced functional materials with customized properties often requires the use of an alloy. This approach has been used for decades, but only recently to create van der Waals (vdW) alloys for applications in electronics, optoelectronics, and thermoelectrics. A route to engineering their physical properties is by mixing isoelectronic elements, as done for the $SnSe_{2(1-x)}S_{2x}$ alloy. Here, by experiment and first-principles modeling, it is shown that the value of x can be adjusted over a wide range, indicating good miscibility of the SnS_2 and $SnSe_2$ compounds. The x-dependence of the indirect bandgap energy from E_{ind} = 1.20 eV for $SnSe_2$ to E_{ind} = 2.14 eV for SnS_2, corresponds to a large bowing coefficient $b \approx 1$ eV, arising from volume deformation and charge exchange effects due to the different sizes and orbital energies of the S- and Se-atoms. This also causes composition-dependent phonon energy modes, electron–phonon interaction, and temperature dependence of E_{ind}. The alloys are exfoliable into thin layers with properties that depend on the composition, but only weakly on the layer thickness. This work shows that the electronic and vibrational properties of the $SnSe_{2(1-x)}S_{2x}$ alloy and its thin layers provide a versatile platform for development and exploitation.

1. Introduction

Tin disulfide (SnS_2) and diselenide ($SnSe_2$) belong to the IV–VI group of van der Waals (vdW) crystals and exist in different polytypes.[1–4] For the polytype phase 2H-MX_2 (metal M = Sn; and chalcogen X = S, Se), the hexagonal unit cell consists of two weakly coupled vdW layers along the *c*-axis and strong covalent metal-chalcogen bonds within each layer (**Figure 1**a).[1–4] These crystals can be produced at low-cost, in part due to the natural abundance of Sn, S, and Se; they are environmentally friendly, and have potential for applications in electronics, optoelectronics, and thermoelectrics.[5–14] Single-layer and multilayer nanosheets of the binary compounds SnS_2 and $SnSe_2$ can be synthesized or isolated from their bulk counterparts by mechanical exfoliation.[15–23] Both bulk SnS_2 and $SnSe_2$ crystals have an indirect bandgap and their in-plane lattice constants, interlayer distances and interlayer binding energies tend to be weakly dependent on the layer thickness.[20] An alternative route to engineering physical properties, such as the bandgap energy, is by varying the composition of the ternary alloy $SnSe_{2(1-x)}S_{2x}$.[24–29] Although SnS_2 and $SnSe_2$ have been widely studied, the electronic properties of the $SnSe_{2(1-x)}S_{2x}$ alloy and their dependence on the layer thickness, alloy composition, temperature, and/or applied strain are

Dr. Z. R. Kudrynskyi, J. Sutcliffe, Dr. M. A. Bhuiyan, Dr. O. Makarovsky, Prof. L. Eaves, Prof. A. Patanè
School of Physics and Astronomy
University of Nottingham
Nottingham NG7 2RD, UK
E-mail: amalia.patane@nottingham.ac.uk

X. Wang, Prof. L. Zhang
Key Laboratory of Automobile Materials of MOE and College of Materials Science and Engineering
Jilin University
2699 Qianjin Str., 130012 Changchun, China
E-mail: lijun_zhang@jlu.edu.cn

The ORCID identification number(s) for the author(s) of this article can be found under https://doi.org/10.1002/adfm.201908092.

DOI: 10.1002/adfm.201908092

Dr. Y. Fu
College of Physics
Jilin University
2699 Qianjin Str., 130012 Changchun, China

Dr. Z. Yang
International MegaGauss Science Laboratory
Institute for Solid State Physics
The University of Tokyo
Kashiwa 277-8581, Japan

Dr. A. Solomon, Prof. V. T. Maslyuk
Institute of Electron Physics
The National Academy of Sciences of Ukraine
Uzhhorod 88017, Ukraine

Prof. Z. D. Kovalyuk
Institute for Problems of Materials Science
The National Academy of Sciences of Ukraine
Chernivtsi Branch, Chernivtsi 58001, Ukraine

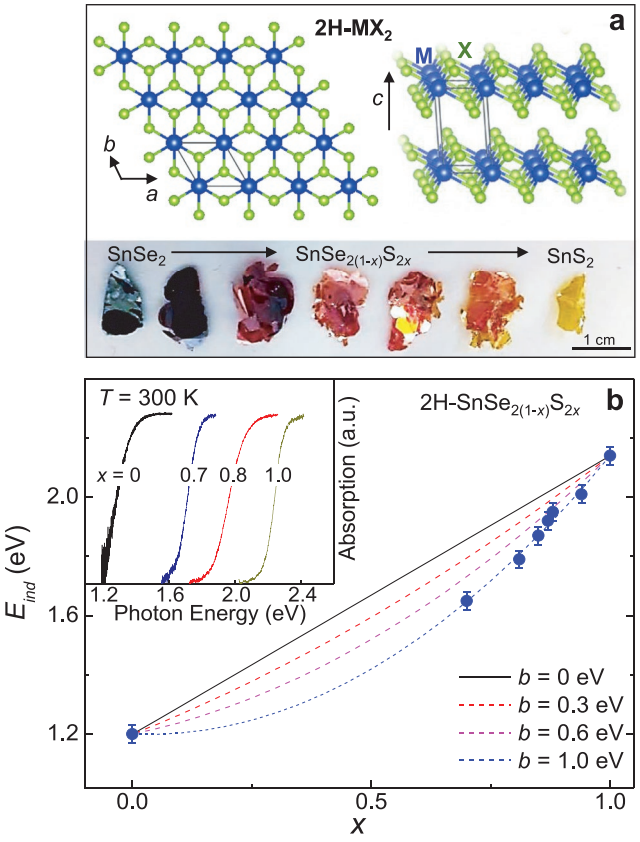

Figure 1. a) Crystal structure for MX_2 (M = Sn and X = Se, S) and optical images of CVT-grown $SnSe_{2(1-x)}S_{2x}$ alloys. b) Dependence of the indirect bandgap energy of $SnSe_{2(1-x)}S_{2x}$ as derived from the measured absorption spectra at $T = 300$ K. The lines show the calculated empirical dependence of the bandgap energy on x, as derived from Equation (1) in the main text with different bowing parameters b. Inset: representative absorption spectra at $T = 300$ K.

presently largely unknown. Furthermore, some of these properties can depend on the specific method of synthesis,[24,28] which can produce materials with different polytype phases and/or stoichiometry.

This work reports on a theoretical and experimental study of 2H-$SnSe_{2(1-x)}S_{2x}$ thin films prepared by a chemical vapor transport (CVT) method. We show that their near band edge absorption energy blueshifts with increasing the S-content, corresponding to a large bowing coefficient $b \approx 1$ eV. The shift is accompanied by an increase of the energy of the optically active Raman phonon modes and a stronger temperature dependence of the bandgap energy, indicative of a composition-dependent electron–phonon interaction. Using first-principles calculations of the electronic structure, we show that these effects arise primarily from the large difference in the atomic radii and atomic orbital energies of the Se and S atoms. The layers are optically active at room temperature with a bandgap energy that depends on the alloy composition, but only weakly on the layer thickness. Thus, the $SnSe_{2(1-x)}S_{2x}$ alloy enables access to a class of low-dimensional semiconductors with a useful range of electronic, optical, and vibrational properties tunable by the alloy composition.

2. Results and Discussion

2.1. Bandgap Energy and Bowing Coefficient

Single crystals of $SnSe_{2(1-x)}S_{2x}$ ($0 \le x \le 1$) were grown by the CVT reaction method within a quartz ampoule using stoichiometric concentrations of high purity (≥ 99.999%) reactants (Sn, S, and Se) and iodine I_2 as the transport agent (see Experimental Section). The as-grown crystals have the shape of flat platelets with mirror-like surfaces and in-plane areas of up to ≈ 1 cm^2 (Figure 1a). They have thickness L of up to ≈ 100 µm and can be readily exfoliated mechanically into nanometer-thick layers with a uniform composition x, as measured by energy-dispersive X-ray (EDX) spectroscopy (**Table 1** and Table S1, Supplementary Information). The nominal composition of the alloys was set to $x_n = 0$, 0.5, 0.70, 0.75, 0.80, 0.85, 0.95, and 1.00. However, the real composition was found to be higher in the ternary compounds (x = 0, 0.70, 0.81, 0.85, 0.87, 0.88, 0.94, and 1.00). At a given growth temperature, S and Se have different vapor pressures. This can affect their transport within the ampoule, causing a deviation of the nominal stoichiometry from the real one.

Figure 1b shows the normalized optical absorption spectra at room temperature (T = 300K) for $SnSe_{2(1-x)}S_{2x}$ films of thickness $t \approx 10$ µm. The absorption edge shifts to higher energies with increasing x. We estimate the indirect bandgap energy, E_{ind}, (Table 1) by plotting the square root of the absorption coefficient, α, versus the photon energy, $h\nu$, and extrapolating the linear part of the $\alpha(h\nu)$ curve to zero. Figure 1b shows the x-dependence of E_{ind} and its fit by the equation

$$E_{ind}(x) = xE_{ind}(SnS_2) + (1-x)E_{ind}(SnSe_2) - bx(1-x) \quad (1)$$

where E_{ind} (SnS_2) = (2.14 ± 0.03) eV and E_{ind}($SnSe_2$) = (1.20 ± 0.03) eV are the measured energy values of the indirect bandgap for SnS_2 and $SnSe_2$, respectively, and b is the bowing coefficient. The data are well described by Equation (1) with b = (1.0 ± 0.1) eV.

We compare our values of E_{ind} and b with those from the literature. For $SnSe_{2(1-x)}S_{2x}$ alloys synthesized by the solvothermal method, E_{ind}(SnS_2) = 2.23 eV, E_{ind}($SnSe_2$) = 1.29 eV

Table 1. Indirect bandgap energy, E_{ind}, and PL peak energy for bulk $SnSe_{2(1-x)}S_{2x}$ (T = 300K). E_{ind} is estimated from a fit to the band edge absorption. The composition x of the alloy is assessed by EDX and compared with the nominal composition x_n.

Nominal composition	Measured composition	E_{ind} [eV]	PL peak energy [eV]
$x_n = 1.00$	$x = 1.00$	2.14 ± 0.03	1.35 ± 0.03
$x_n = 0.95$	$x = 0.94$	2.01 ± 0.03	1.69 ± 0.04
$x_n = 0.85$	$x = 0.88$	1.95 ± 0.03	1.66 ± 0.02
$x_n = 0.80$	$x = 0.87$	1.92 ± 0.03	1.64 ± 0.02
$x_n = 0.75$	$x = 0.85$	1.87 ± 0.03	1.61 ± 0.03
$x_n = 0.70$	$x = 0.81$	1.79 ± 0.03	1.63 ± 0.02
$x_n = 0.50$	$x = 0.70$	1.65 ± 0.03	1.58 ± 0.01
$x_n = 0$	$x = 0$	1.20 ± 0.03	1.16 ± 0.01

and $b = 0.03$ eV;[25] for CVT-grown crystals, $E_{ind}(SnS_2) = 2.27$ eV, $E_{ind}(SnSe_2) = 1.37$ eV and $b = 1.1$ eV.[28] Differences in the measured values of E_{ind} and b can be caused by the coexistence of different polytype phases and/or stoichiometries, and a deviation of the real composition x from the nominal one. The composition x of the alloy is measured by EDX with an accuracy of ± 1% (Table 1). To assess the polytype phase of our compounds, we use Raman spectroscopy. The Raman spectra reveal the characteristic A_{1g} and E_g Raman modes of 2H-$SnSe_{2(1-x)}S_{2x}$ (Supporting Information S2). The X-ray diffraction (XRD) studies give lattice constants consistent with the 2H polytype phase of $SnSe_2$ and SnS_2 (Supporting Information S3).

The assessment of both crystal structure and composition of the alloy enables a reliable comparison between the measured bowing coefficient and that calculated using first-principles calculations. We start our modeling by investigating the stability of the 2H-$SnSe_{2(1-x)}S_{2x}$ alloy using the state-of-the-art cluster expansion (CE) approach.[30,31] The formability of the alloy is evaluated by calculating its formation enthalpy ΔH:

$$\Delta H = \left[E\left(SnSe_{2(1-x)}S_{2x}\right) - xE\left(SnS_2\right) - (1-x)E\left(SnSe_2\right)\right]/2 \qquad (2)$$

where $E(SnS_2)$, $E(SnSe_2)$, and $E(SnSe_{2(1-x)}S_{2x})$ represent the enthalpies of SnS_2, $SnSe_2$, and their mixed alloy, respectively. As shown in **Figure 2**a, at different x the formation enthalpy is always positive and is small ($\Delta H < 25$ meV per anion), implying a tendency to solid solution miscibility. In particular, our calculations show that, for all values of x, the highest miscibility temperature is below $T = 180$ K (Figure 2b). In our enthalpy calculations in the mean-field approximation, we neglect the lattice vibration contribution. This may lead to an underestimation of the solubility and thus an overestimation of the miscibility temperature. To study the electronic structure of the 2H-$SnSe_{2(1-x)}S_{2x}$ alloy, we employ the "special quasi-random structure" (SQS) approach,[32,33] which takes into account disorder effects for a random alloy in periodic supercell calculations. The modified Becke Johnson (MBJ)[34] exchange-correlation functional was used to remedy the self-interaction error in density functional theory (DFT) calculations. Figure 2c shows the calculated x-dependence of the bandgap energy and its comparison with the measured one: it can be seen that besides reproducing the measured values of the indirect bandgap energy of $SnSe_2$ and SnS_2, our model is in good agreement with the experimental observation of a large bowing coefficient b ($b \approx 1$ eV, Figure 2d). This is significantly larger than that for several covalent (non-vdW) alloys, such as CdS_xSe_{1-x} ($b = 0.3$ eV)[35] and ZnS_xSe_{1-x} ($b = 0.41$–0.63 eV),[36,37] and for vdW alloys, such as $MoS_{2(1-x)}Se_{2x}$ ($b \approx 0.5$ eV)[38–40] and $WS_{2(1-x)}Se_{2x}$ ($b = 0.04$ eV)[38] (see the Supplementary Information S4 for the values of the bandgap bowing coefficient measured or calculated for different alloys in the literature).

To understand the physical origin of the large optical bandgap bowing and its composition dependence, we examine the distinct contributions to b due to volume deformation (b_{VD}), charge exchange (b_{CE}), and structural relaxation (b_{SR}), i.e., $b = b_{VD} + b_{CE} + b_{SR}$.[41,42] The b_{VD}-term takes into account a change in the bandgap due to the compression (dilation) of the $SnSe_2$ (SnS_2) lattice parameters in the alloy; the b_{CE}-term

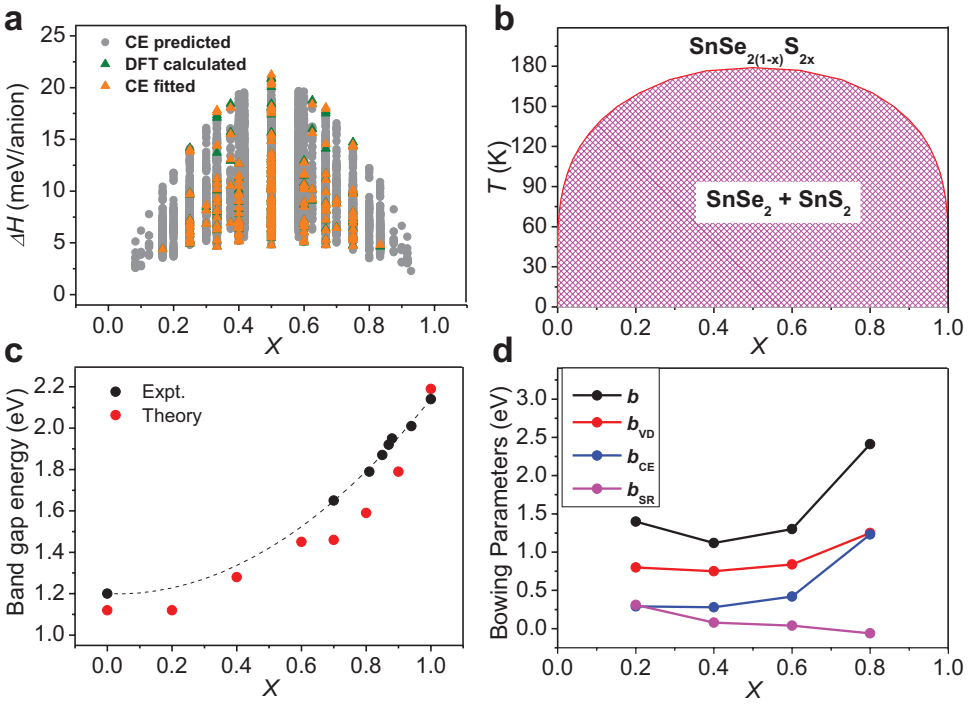

Figure 2. a) Calculated formation enthalpies (ΔH) of $SnSe_{2(1-x)}S_{2x}$ alloys using the CE approach. The different colors show the DFT-calculated, CE-fitted, and CE-predicted data. b) Simulated phase diagram of the $SnSe_{2(1-x)}S_{2x}$ alloy. The area of phase separation is shaded. c) Measured (black) and calculated (red) values of the bandgap energy of $SnSe_{2(1-x)}S_{2x}$ alloys as a function of x. The dashed line is the bandgap energy from Equation (1) with $b = 1$ eV. d) Dependence on x of the calculated total bandgap bowing parameters (b) and the three contributing terms (b_{VD}, b_{CE}, and b_{SR}).

is calculated from the change in the orbital energies of the Se and S atoms; and the b_{SR}-term represents the change when moving from the atomically unrelaxed to the relaxed alloy. As shown in Figure 2d, the total bowing coefficient shows a clear composition dependence, significantly stronger at larger x. At first glance, the large bandgap bowing parameter of the vdW $SnSe_{2(1-x)}S_{2x}$ alloy could be attributed entirely to the different sizes and orbital energies of the S- and Se-atoms forming the alloy. However, other (Se, S) alloys in the literature have revealed small bowing parameters.[35–40] To fully explain the large bowing parameter in the $SnSe_{2(1-x)}S_{2x}$ alloy, we should consider its specific crystal structure (Figure 1a). This is an essential factor leading to a non-linear dependence of the electronic structure of the alloy on composition. The strongest contribution to the value of b arises from volume deformation due to the substantial lattice mismatch between SnS_2 and $SnSe_2$; also, charge transfer due to the different orbital energies of the S and Se atoms plays an important role. Both effects become more prominent at large x and account for the calculated composition-dependent bowing coefficient. The weak structural relaxation contribution can be understood by the nearly linear dependence of the lattice parameters on x, which follows Vegard's law (Supporting Information S5).

2.2. Electron–Phonon Interaction

We examine further the properties of the alloy by temperature-dependent studies of the absorption spectra. As shown in **Figure 3**, over the range T = 5–300 K, the T-dependence of the indirect bandgap energy is well described by the O'Donnell–Chen model, which takes into account the lattice expansion and electron–phonon interaction:[43]

$$E_{ind}(T) = E_{ind}(0) - S\langle\hbar\omega\rangle\left[\coth\left(\langle\hbar\omega\rangle/2k_BT\right) - 1\right] \quad (3)$$

Here E_{ind} (0) is the indirect bandgap at T = 0K, $\langle\hbar\omega\rangle$ is an average phonon energy, S is a dimensionless constant describing the electron–phonon coupling, and k_B is the Boltzmann constant.

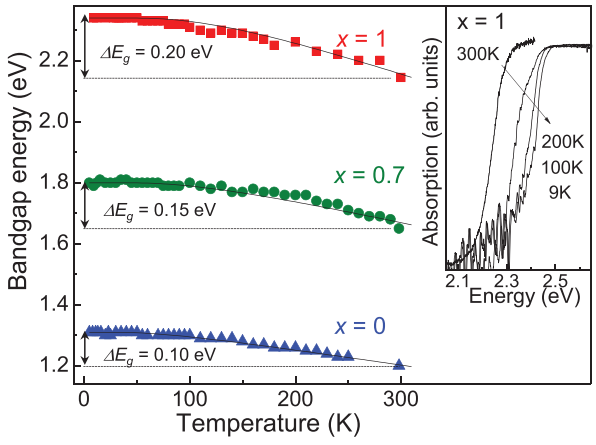

Figure 3. Temperature dependence of the bandgap energy for CVT-grown $SnSe_{2(1-x)}S_{2x}$ alloys. The solid black lines show fits to the experimental data by the O'Donnell–Chen equation. Inset: representative absorption spectra for SnS_2 at different temperatures.

Table 2. Parameters from the O'Donnell–Chen model describing the temperature (T) dependence of the indirect bandgap energy and its change, ΔE, from T = 0 to 300 K. E_{ind} (0) is the indirect bandgap at T = 0 K, $\langle\hbar\omega\rangle$ is an average phonon energy, and S is a dimensionless constant describing the electron–phonon coupling.

Measured composition	$E_{ind}(0)$ [eV]	$\langle\hbar\omega\rangle$ [meV]	S	ΔE [eV]
x = 1.0	2.34	32.2	7.0	0.20
x = 0.7	1.80	27.8	4.5	0.15
x = 0.0	1.31	18.4	3.0	0.11

Each solid line in Figure 3 is the fit to the $E_{ind}(T)$ data using Equation (3) with $E_{ind}(0)$ and S as fitting parameters, and by fixing the average phonon energy $\langle\hbar\omega\rangle$ to the value derived from the frequencies of the Raman active modes for each compound (**Table 2** and Supporting Information S2). The frequencies of the A_{1g} and E_g Raman modes for $SnSe_2$ (184.0 and 116.8 cm^{-1}) are significantly smaller than for SnS_2 (313.2 and 202–212 cm^{-1}) due to the lighter atomic mass of S compared to that of Se (the mass ratio m_S/m_{Se} is ≈ 0.4). Correspondingly, the average phonon energy $\langle\hbar\omega\rangle$ decreases from about 32 meV in SnS_2 to 18 meV in $SnSe_2$. However, although the phonon frequencies in SnS_2 are the highest among the $SnSe_{2(1-x)}S_{2x}$ alloys, the SnS_2 binary compound exhibits the strongest dependence of the bandgap energy on temperature. In particular, for x = 1, the electron–phonon coupling parameter is S = 7 and is larger than in $SnSe_{2(1-x)}S_{2x}$ with x = 0.7 (S = 4.5) and x = 0 (S = 3).

The stronger electron–phonon coupling at larger x is supported by our model. We use the density functional perturbation approach[44] to examine the electron–phonon interaction in $SnSe_2$ and SnS_2. Our electronic band structure calculations (**Figure 4**a,b) show that for both compounds the conduction band minimum (blue line) is located along the L–M line in the Brillouin zone. The valence band maximum (red line) is instead along the Γ–M line. This is consistent with angle-resolved photoemission spectroscopy measurements on SnS_2, which indicate a valence band maximum in proximity of the Γ point along the Γ–M line.[6] The calculated phonon spectra (Figure 4c,d) exhibit no imaginary modes and SnS_2 has generally higher phonon frequencies than $SnSe_2$ due to the stronger Sn—S bonding and the lighter mass of S. The electron—phonon coupling matrix elements $|g_{mn,v}(k, q)|$ are calculated along the high-symmetry directions in the Brillouin zone of phonon wavevector q and electron wavevector k at Γ. Here, m and n refer to the conduction band minimum (Figure 4e,f) and valence band maximum (Figure 4g,h), and v represents the phonon mode type. It can be seen that the electron—phonon coupling matrix elements for SnS_2 (Figure 4e,g) are larger than those for $SnSe_2$ (Figure 4f,h). We assign this to the stronger Sn—S covalent bonding compared to Sn—Se, as is evident from the charge density difference plots, showing a stronger electron localization along the Sn-S bonds (insets of Figure 4e,f). We note that our calculations of the bandgap energy (Figure 2) assume a static lattice. The stronger electron—phonon interaction at large x may contribute to the composition dependence of the bandgap energy. This may account for the discrepancy between the measured and calculated bowing coefficients at large x (Figure 2c).

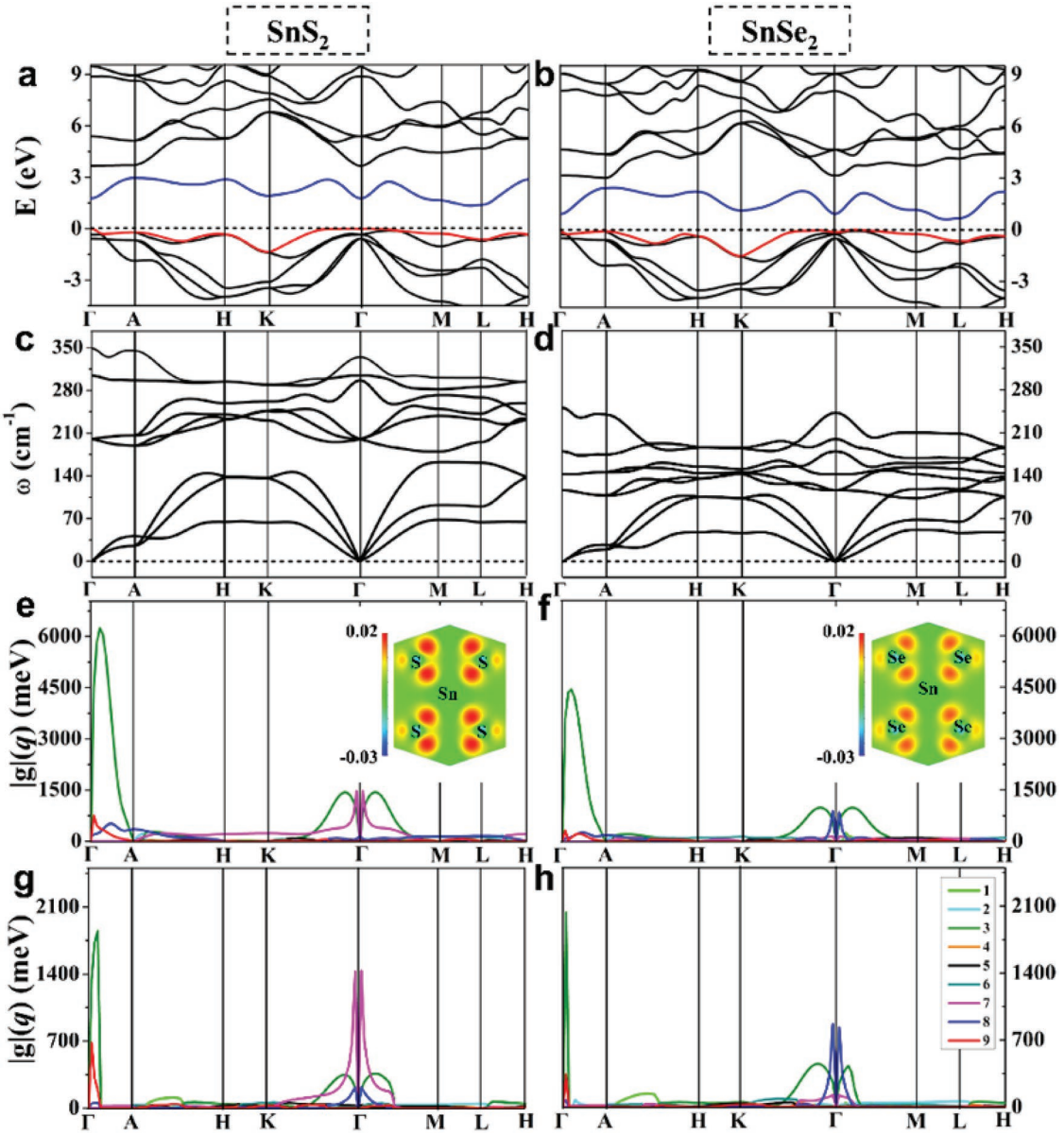

Figure 4. a,b) Calculated electronic band structures of a) SnS_2 and b) $SnSe_2$. The lowest conduction band is indicated in blue and the highest valence band in red. c,d) Phonon dispersion curves of SnS_2 and $SnSe_2$. e–h) Calculated electron–phonon matrix elements. e,f) The calculations were performed for the lowest conduction band and g,h) the highest valence band. The contributions from all the phonon modes are calculated. Inset: electron charge density difference of SnS_2 and $SnSe_2$, respectively. The charge accumulation and depletion are indicated in red and blue, respectively.

2.3. Photoluminescence

All our alloys are optically active at room temperature with a photoluminescence (PL) emission that shifts to high energy with increasing x (Table 1). As shown in **Figure 5**, the PL emission band blueshifts to higher energy and broadens going from $x = 0$ to 0.9. Also, its Stokes-shift, as measured relative to the absorption edge (red arrows in Figure 5) increases with x. However, for $x = 1$, we observe a different behavior: the PL band exhibits an unusually large redshift (≈ 0.8 eV) relative to the absorption edge; also, the PL emission is at a lower energy than that of alloys with a lower x. These observations suggest a dominant recombination of carriers from deep levels and/or regions of the alloy with a different stoichiometry. Although our Raman studies do not reveal the coexistence of different stoichiometries, we do not exclude that local inclusions of SnS in SnS_2 may be responsible for the PL emission in this sample. A PL emission near 1.4 eV was previously reported for thick layers of SnS_2 and ascribed to band-to-band transitions in SnS regions.[45] We observe a similar behavior in our samples. The PL band in our SnS_2 samples is centered at ≈1.35 eV, which is in good agreement with the value of the direct bandgap of SnS, $E_{g,dir}$(SnS) = 1.36 eV.[45] We exclude the possibility that such regions with different stoichiometry are generated upon laser excitation as the PL spectra were always measured at low excitation power densities ($P < 10$ μW μm^{-2}) to avoid excessive

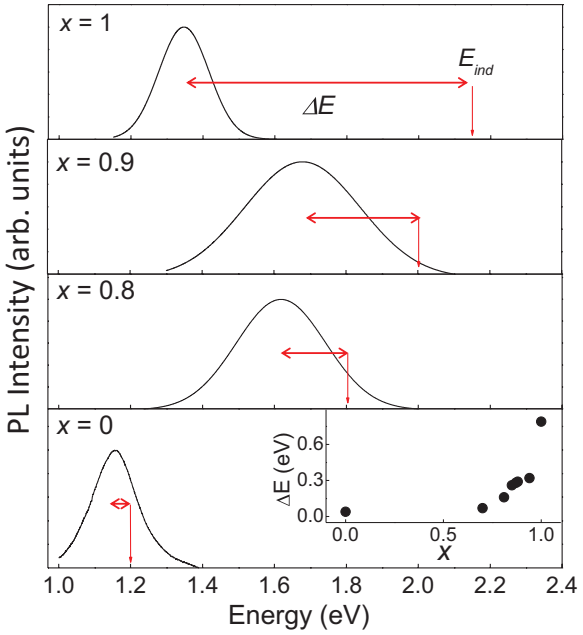

Figure 5. Room temperature PL for $SnSe_{2(1-x)}S_{2x}$ films. The redshift, ΔE, of the PL emission peak relative to the absorption edge is indicated by red arrows. The dependence of ΔE on x is shown in the inset.

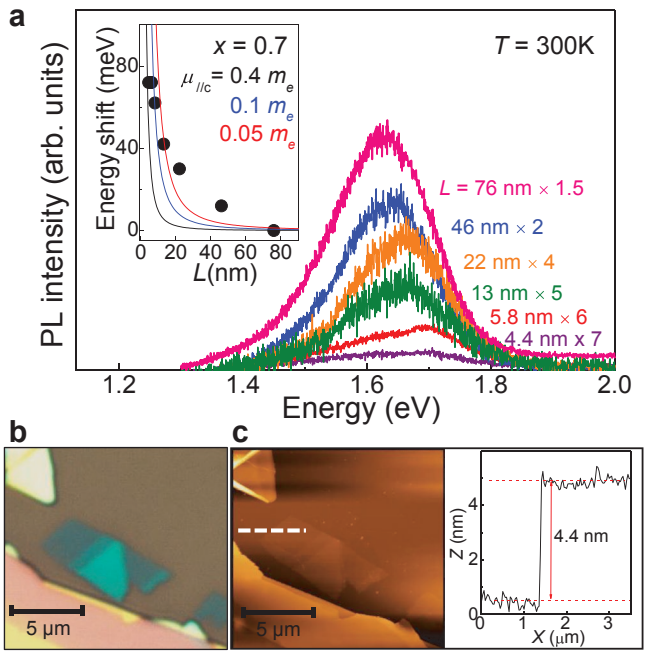

Figure 6. a) Room-temperature PL for $SnSe_{2(1-x)}S_{2x}$ films of different thickness L ($x = 0.7$). The inset shows the measured energy shift of the PL peak energy versus the layer thickness and the calculated dependence using a 2D quantum well model in the effective mass approximation with different exciton reduced masses. b) Optical and c) AFM images of $SnSe_{2(1-x)}S_{2x}$ films with different layer thickness L. The inset is the AFM Z-profiles obtained along the dotted line shown in part (c).

lattice heating. Also, there was no indication of degradation or changes of the flakes during the measurements. Thus, our findings are different from those reported in the literature showing a structural transformation of SnS_2 into SnS by electron beam irradiation.[45,46] Regions of our samples with a lower chalcogen concentration are most likely caused by a non-uniform crystal growth. These can be present in both SnS_2 and $SnSe_2$ compounds, as well as their alloys. However, the resulting Stokes shift is more prominent in SnS_2 and S-rich alloys due to the larger difference between the bandgap values of the Sn-sulfides compared to that for the Sn-selenides.[45,47]

2.4. Quantum Confinement Effects

Our experimental and theoretical study of the $SnSe_{2(1-x)}S_{2x}$ alloy indicates that the electronic and vibrational properties of the alloy are strongly dependent on the alloy composition. In this section, we examine the role of quantum confinement in the exfoliated flakes of the alloys. **Figure 6**a–c shows the room temperature micro-PL (μPL) emission spectra and images of mechanically exfoliated nanosheets of $SnSe_{2(1-x)}S_{2x}$ ($x = 0.7$) with thicknesses L from ≈ 4 to ≈100 nm. The atomic force microscopy (AFM) images indicate that the exfoliated flakes are almost flat on the atomic scale with an average surface roughness of less than 1 nm along the c-axis (Figure 6c). With decreasing L, the μPL emission tends to shift to high energy and its intensity decreases. No PL signal was detected in layers thinner than ≈ 4 nm. In spite of variations from flake to flake, the shift and quenching of the PL at small L is always observed, but is generally small (<100 meV). In order to avoid any potential damage of the flakes by the laser beam through excessive lattice heating, the PL spectra were measured at low excitation power densities ($P < 10$ μW μm^{-2}). No degradation of the flakes was observed during the measurements, suggesting that they are not sensitive to air. As can be seen from Figure 6a, the intensity of the PL signal decreases with decreasing layer thickness. This is expected from a reduction in the thickness of the optically absorbing material. The absence of PL emission in flakes thinner than ≈ 4 nm is most likely due to the fact that the signal for such thin flakes is too low to be distinguished from the background signal. We note that in contrast to thin layers of III–VI compounds, such as InSe,[48] in these VI–VI compounds a simple model of a square quantum well potential of infinite height, giving a PL emission peak at $h\nu = h\nu_{3D} + \pi^2\hbar^2/2L^2\mu_{//c}$, does not provide a good fit to the measured data (see lines in the inset of Figure 6a). Here $h\nu_{3D}$ is the measured PL peak energy in the bulk and $\mu_{//c}$ is the reduced exciton mass along the c-axis. Also, an energy shift of the PL emission peak is observed in $SnSe_{2(1-x)}S_{2x}$ layers that are relatively thick ($L > 20$ nm). A similar behavior was reported in other vdW materials, such as GeS.[49] An energy shift for such thick layers cannot be explained by assuming a simple quantum well model, as the corresponding value of the reduced exciton mass would be unrealistically small (Figure 6a,inset). However, we note that the PL emission can be influenced by carrier relaxation into/recombination from localized states in the layer plane, resulting in a Stokes shift of the PL emission with respect to the absorption (Figure 5). Thus, the PL emission peak energy may not reflect accurately quantum confinement effects. Other effects can also play a role. We suggest that the weak dependence of the PL emission energy on the layer thickness at small L (<20 nm) can be influenced, for example, by a reduction of the screening of electrostatic interactions, and by

the large electron and hole band edge masses. In these binary compounds the nature of the bandgap remains indirect for the single monolayer thickness, but excitonic effects may be strongly enhanced due to quantum confinement and reduced dielectric screening.[20] The increase of the exciton binding energy with decreasing layer thickness can contribute to a weaker energy shift of the PL emission than expected from a simple 2D quantum well model, which requires further research.

3. Conclusions

In summary, the optical absorption spectra of the $SnSe_{2(1-x)}S_{2x}$ alloy vary over an extended energy range from the near-infrared to the visible range, with a large bowing parameter that depends on the alloy composition. The value of x can be tuned over a wide compositional range, indicating a good miscibility of the SnS_2 and $SnSe_2$ compounds. The measured temperature dependence of the bandgap energy is well described by the O'Donnell–Chen model and indicates an electron–phonon coupling that increases with the S-content. The room temperature miscibility behavior, large bowing parameter, and composition-dependent electron–phonon coupling are reproduced by first-principles modeling. The underlying mechanism is attributed to the different sizes and orbital energies of S and Se forming the alloy. In addition, we have observed a blueshift of the PL emission in thin exfoliated flakes due to quantum confinement. Electron–phonon interactions and quantum confinement affect the operation of electronic and optical devices by controlling the electrical resistivity, optical absorption, thermalization of hot carriers, thermoelectric properties, etc. Thus, the ternary vdW alloy and its thin layers provide a promising material platform to investigate and exploit further.

4. Experimental Section

Single crystals of $SnSe_{2(1-x)}S_{2x}$ ($0 \le x \le 1$) were grown by the CVT reaction method within a quartz ampoule. The ampoule was kept in a furnace with a temperature gradient from $T = 650$ to 500 °C over a length of ≈10 cm: the reactants were introduced in the hot region of the furnace tube and they crystallize in the cooler region over a period of 24 h.

The experimental set-up for μPL and Raman measurements comprised a He–Ne laser ($\lambda = 633$ nm) and a frequency-doubled Nd:YVO_4 laser ($\lambda = 532$ nm), an XY linear positioning stage, an optical confocal microscope system, and a spectrometer with 150 and 1200 grooves/mm gratings, equipped with a charge-coupled device (CCD). For the room temperature studies, the laser beam was focused to a diameter $d \approx 1$ μm using a 100 × objective and the μPL spectra were measured at low power densities ($P < 10^3$ W cm^{-2}) to avoid lattice heating.

Optical absorption spectra were measured in the temperature range $T = 5$–300 K. White light from a 7W halogen lamp (HL-2000-FSHA from Ocean Optics) was transmitted via an optical fiber through $SnSe_{2(1-x)}S_{2x}$ films of thickness $t \approx 10$ μm and collected by a spectrometer equipped with a CCD array (USB4000-UV-VIS from Ocean Optics). For the temperature-dependent studies, the samples were mounted in a cryostat with optical windows.

The alloys were examined by EDX spectroscopy using a JEOL-JSM-6610LV scanning electron microscope fitted with an Oxford Instruments X-Max 800 mm energy-dispersive spectrometer. Images of the $SnSe_{2(1-x)}S_{2x}$ flake topography were acquired by AFM in non-contact mode under ambient conditions.

First-principles calculations were performed within the framework of DFT by using the projected augmented wave pseudo-potential method as implemented in the Vienna Ab-initio Simulation Package code.[50,51] The generalized gradient approximation formulated by Perdew, Burke, and Ernzerhof[52,53] was used as exchange correlation functional. The kinetic energy cut-off for the plane wave basis was chosen to be 340 eV, with k-point grid spacing set to $2\pi \times 0.04$ Å^{-1} for electronic Brillouin zone integration. Geometry optimizations (including cell parameters and internal atomic positions) were performed using the conjugate gradient technique, until the residual force converged to below 0.05 eV Å^{-1}. To properly treat the vdW interaction in the current layered system, the optB86b-vdW[54,55] functional was adopted, which gives a satisfactory description of the Sn–S systems.[56,57] As shown in Table S2 in the Supplementary Information, the optimized lattice parameters of SnS_2 and $SnSe_2$ show good agreement with the experimental values. To remedy the self-interaction error of DFT calculations, two exchange-correlation functionals were employed, i.e., the MBJ[34] and hybrid (HSE)[58] forms, both of which give good agreement of the bandgap values of SnS_2 and $SnSe_2$ with the experimental ones (Table S2, Supplementary Information). The formability and miscibility temperature of 2H-$SnSe_{2(1-x)}S_{2x}$ alloys were evaluated by using the state-of-the-art CE approach,[30,31] as implemented in the Alloy Theoretic Automated Toolkit code.[59] The electronic structures of the 2H-$SnSe_{2(1-x)}S_{2x}$ alloys were calculated by the SQS approach[32,33] that takes into account disorder effects for a random alloy in periodic supercell calculations. The electronic structure, phonon spectra, and electron–phonon coupling for SnS_2 and $SnSe_2$ were calculated by using the density functional perturbation approach together with the maximally localized Wannier function, as integrated in the Quantum ESPRESSO package.[60,61] For these calculations, the energy cut-off for wavefunction expansion was chosen to be 40 Ry. A 6 × 6 × 6 Γ-centered k-point grid and a 6 × 6 × 6 Γ-centered q-point grid was adopted for electronic structure and phonon calculations, respectively. The electron–phonon matrix elements $|g_{mn,\nu}(k,q)|$ associated with the electronic wavefunction and the change of the self-consistent potential were calculated by using 6 × 6 × 6 electron and phonon grids k centered at Γ. Here, m and n refer to the electron band indexes and ν represents the phonon mode type. Since SnS_2 and $SnSe_2$ are polar materials, the non-zero Born effective charges were considered in order to correctly treat the long-range interaction in the crystal.

Supporting Information

Supporting Information is available from the Wiley Online Library or from the author.

Acknowledgements

Z.R.K. and X.W. contributed equally to this work. This work was supported by the Engineering and Physical Sciences Research Council (grant numbers EP/M012700/1 and EP/L022494/1); The University of Nottingham; The National Academy of Sciences of Ukraine; The Leverhulme Trust (RF-2017-224); the European Union's Horizon 2020 research and innovation programme Graphene Flagship Core 2 (grant number 785219); and the Chinese Academy of Sciences. The work at Jilin University is supported by the National Natural Science Foundation of China (grant numbers 61722403 and 11674121), Jilin Province Science and Technology Development Program (grant number 20190201016JC), and Program for Jilin University Science and Technology Innovative Research Team. Calculations were performed in part at the high-performance computing center of Jilin University. The authors also thank the Nanoscale and Microscale Research Centre (nmRC) for

providing access to the instrumentation for EDX studies. Also, the authors thank Rebeka Hall and Peter Fletcher for their contribution to the preliminary studies.

Conflict of Interest

The authors declare no conflict of interest.

Keywords

electron-phonon interaction, semiconducting alloys, $SnSe_{2(1-x)}S_{2x}$, van der Waals crystals

Received: September 30, 2019
Revised: November 25, 2019
Published online:

[1] R. H. Williams, R. B. Murray, D. W. Govan, J. M. Thomas, E. L. Evans, *J. Phys. C: Solid State Phys.* **1973**, *6*, 3631.
[2] R. S. Mitchell, Y. Fujiki, Y. Ishizawa, *Nature* **1974**, *247*, 537.
[3] B. Pałosz, S. Gierlotka, F. Levy, *Acta Crystallogr., Sect. C: Cryst. Struct. Commun.* **1985**, *41*, 1404.
[4] B. Pałosz, W. Steurer, H. Schulz, *Acta Crystallogr., Sect. B: Struct. Sci.* **1990**, *46*, 449.
[5] J. Smith, P. E. Meek, W. Y. Liang, *J. Phys. C: Solid State Phys.* **1977**, *10*, 1321.
[6] Y. Huang, E. Sutter, J. T. Sadowski, M. Cotlet, O. L. A. Monti, D. A. Racke, M. R. Neupane, D. Wickramaratne, R. K. Lake, B. A. Parkinson, P. Sutter, *ACS Nano* **2014**, *8*, 10743.
[7] B.-Z. Sun, Z. Ma, C. He, K. Wu, *Phys. Chem. Chem. Phys.* **2015**, *17*, 29844.
[8] B.-Z. Sun, Z.-J. Ma, C. He, K.-C. Wu, *Phys. Chem. Chem. Phys.* **2015**, *17*, 29844.
[9] L. A. Burton, T. J. Whittles, D. Hesp, W. M. Linhart, J. M. Skelton, B. Hou, R. F. Webster, G. O'Dowd, C. Reece, D. Cherns, D. J. Fermin, T. D. Veal, V. R. Dhanak, A. Walsh, *J. Mater. Chem. A* **2016**, *4*, 1312.
[10] Y. Ding, B. Xiao, G. Tang, J. Hong, *J. Phys. Chem. C* **2017**, *121*, 225.
[11] Y. Gong, H. Yuan, C.-L. Wu, P. Tang, S.-Z. Yang, A. Yang, G. Li, B. Liu, J. van de Groep, M. L. Brongersma, M. F. Chisholm, S.-C. Zhang, W. Zhou, Y. Cui, *Nat. Nanotechnol.* **2018**, *13*, 294.
[12] T. S. Pan, D. De, J. Manongdo, A. M. Guloy, V. G. Hadjiev, Y. Lin, H. B. Peng, *Appl. Phys. Lett.* **2013**, *103*, 093108.
[13] X. Zhou, Q. Zhang, L. Gan, H. Li, T. Zhai, *Adv. Funct. Mater.* **2016**, *26*, 4405.
[14] X. Zhou, Q. Zhang, L. Gan, H. Li, J. Xiong, T. Zhai, *Adv. Sci.* **2016**, *3*, 1600177.
[15] J. W. Seo, J. T. Jang, S. W. Park, C. J. Kim, B. W. Park, J. W. Cheon, *Adv. Mater.* **2008**, *20*, 4269.
[16] D. De, J. Manongdo, S. See, V. Zhang, A. Guloy, H. Peng, *Nanotechnology* **2013**, *24*, 025202.
[17] G. Su, V. G. Hadjiev, P. E. Loya, J. Zhang, S. Lei, S. Maharjan, P. Dong, P. M. Ajayan, J. Lou, H. Peng, *Nano Lett.* **2015**, *15*, 506.
[18] J. Xia, D. Zhu, L. Wang, B. Huang, X. Huang, X.-M. Meng, *Adv. Funct. Mater.* **2015**, *25*, 4255.
[19] X. Zhou, L. Gan, W. Tian, Q. Zhang, S. Jin, H. Li, Y. Bando, D. Golberg, T. Zhai, *Adv. Mater.* **2015**, *27*, 8035.
[20] J. Gonzalez, I. Oleynik, *Phys. Rev. B* **2016**, *94*, 125443.
[21] S. Saha, A. Banik, K. Biswas, *Chem.—Eur. J.* **2016**, *22*, 15634.
[22] J. Zeng, E. Liu, Y. Fu, Z. Chen, C. Pan, C. Wang, M. Wang, Y. Wang, K. Xu, S. Cai, X. Yan, Y. Wang, X. Liu, P. Wang, S.-J. Liang, Y. Cui, H. Y. Hwang, H. Yuan, F. Miao, *Nano Lett.* **2018**, *18*, 1410.
[23] R.-J. Chang, H. Tan, X. Wang, B. Porter, T. Chen, Y. Sheng, Y. Zhou, H. Huang, H. Bhaskaran, J. H. Warner, *ACS Appl. Mater. Interfaces* **2018**, *10*, 13002.
[24] V. G. Hadjiev, D. De, H. B. Peng, J. Manongdo, A. M. Guloy, *Phys. Rev. B* **2013**, *87*, 104302.
[25] J. Yu, C.-Y. Xu, Y. Li, F. Zhou, X.-S. Chen, P.-A. Hu, L. Zhen, *Sci. Rep.* **2015**, *5*, 17109.
[26] P. Perumal, R. K. Ulaganathan, R. Sankar, Y.-M. Liao, T.-M. Sun, M.-W. Chu, F. C. Chou, Y.-T. Chen, M.-H. Shih, Y.-F. Chen, *Adv. Funct. Mater.* **2016**, *26*, 3630.
[27] Y. Huang, X. Chen, D. Zhou, H. Liu, C. Wang, J. Du, L. Ning, S. Wang, *J. Phys. Chem. C* **2016**, *120*, 5839.
[28] Y. Wang, L. H. Le Huang, B. Li, J. Shang, C. Xia, C. Fan, H.-X. Deng, Z. Wei, J. Li, *J. Mater. Chem. C* **2017**, *5*, 84.
[29] S. Dong, Z. Wang, *Beilstein J. Nanotechnol.* **2018**, *9*, 1820.
[30] J. M. Sanchez, F. Ducastelle, D. Gratias, *Phys. A: Stat. Mech. Appl.* **1984**, *128*, 334.
[31] J. M. Sanchez, *Phys. Rev. B* **2010**, *81*, 224202.
[32] A. Zunger, S.-H. Wei, L. G. Ferreira, J. E. Bernard, *Phys. Rev. Lett.* **1990**, *65*, 353.
[33] A. van de Walle, P. Tiwary, M. de Jong, D. L. Olmsted, M. Asta, A. Dick, D. Shin, Y. Wang, L.-Q. Chen, Z.-K. Liu, *Calphad* **2013**, *42*, 13.
[34] F. Tran, P. Blaha, *Phys. Rev. Lett.* **2009**, *102*, 226401.
[35] L. A. Swafford, L. A. Weigand, M. J. Bowers, J. R. McBride, J. L. Rapaport, T. L. Watt, S. K. Dixit, L. C. Feldman, S. J. Rosenthal, *J. Am. Chem. Soc.* **2006**, *128*, 12299.
[36] L. G. Suslina, D. L. Fedorov, S. G. Konnikov, F. F. Kodzhespirow, A. A. Andreev, E. G. Shariai, *Fiz. Tekh. Poluprovodn.* **1977**, *11*, 1934; *Sov. Phys. – Semicond.* **1977**, *11*, 1132.
[37] A. Ebina, E. Fukunaga, T. Takahashi, *Phys. Rev. B* **1974**, *10*, 2495.
[38] J. Kang, S. Tongay, J. Li, J. Wu, *J. Appl. Phys.* **2013**, *113*, 143703.
[39] H. Li, X. Duan, X. Wu, X. Zhuang, H. Zhou, Q. Zhang, X. Zhu, W. Hu, P. Ren, P. Guo, L. Ma, X. Fan, X. Wang, J. Xu, A. Pan, X. Duan, *J. Am. Chem. Soc.* **2014**, *136*, 3756.
[40] Q. Feng, N. Mao, J. Wu, H. Xu, C. Wang, J. Zhang, L. Xie, *ACS Nano.* **2015**, *9*, 7450.
[41] S.-H. Wei, A. Zunger, *Phys. Rev. Lett.* **1996**, *76*, 664.
[42] M. Ferhat, F. Bechstedt, *Phys. Rev. B* **2002**, *65*, 075213.
[43] K. P. C. O'Donnell, X. Chen, *Appl. Phys. Lett.* **1991**, *58*, 2924.
[44] F. Giustino, *Rev. Mod. Phys.* **2017**, *89*, 015003.
[45] P. Sutter, H.-P. Komsa, A. V. Krasheninnikov, Y. Huang, E. Sutter, *Appl. Phys. Lett.* **2017**, *111*, 262102.
[46] E. Sutter, Y. Huang, H.-P. Komsa, M. Ghorbani-Asl, A. V. Krasheninnikov, P. Sutter, *Nano Lett.* **2016**, *16*, 4410.
[47] O. Madelung, *Semiconductor: Data Handbook*, Springer, London **2003**, p. 580, Ch. 23.
[48] G. W. Mudd, S. A. Svatek, T. Ren, A. Patanè, O. Makarovsky, L. Eaves, P. H. Beton, Z. D. Kovalyuk, G. V. Lashkarev, Z. R. Kudrynskyi, A. I. Dmitriev, *Adv. Mater.* **2013**, *25*, 5714.
[49] E. Sutter, B. Zhang, M. Sun, P. Sutter, *ACS Nano* **2019**, *13*, 9352.
[50] G. Kresse, J. Furthmüller, *Comput. Mater. Sci.* **1996**, *6*, 15.
[51] G. Kresse, J. Furthmüller, *Phys. Rev. B* **1996**, *54*, 11169.
[52] J. P. Perdew, K. Burke, M. Ernzerhof, *Phys. Rev. Lett.* **1996**, *77*, 3865.
[53] S. Grimme, *J. Comput. Chem.* **2006**, *27*, 1787.

[54] I. Hamada, *Phys. Rev. B* **2014**, *89*, 121103.
[55] J. Klimeš, D. R. Bowler, A. Michaelides, *Phys. Rev. B* **2011**, *83*, 195131.
[56] X. Wang, Z. Liu, X.-G. Zhao, J. Lv, K. Biswas, L. Zhang, *ACS Appl. Mater. Interfaces* **2019**, *11*, 24867.
[57] X. Wang, Y. Li, Y.-X. Pang, Y. Sun, X.-G. Zhao, J.-R. Wang, L. Zhang, *Sci. China: Phys., Mech. Astron.* **2018**, *61*, 107311.
[58] A. V. Krukau, O. A. Vydrov, A. F. Izmaylov, G. E. Scuseria, *J. Chem. Phys.* **2006**, *125*, 224106.
[59] A. van de Walle, M. Asta, G. Ceder, *Calphad* **2002**, *26*, 539.
[60] J. Noffsinger, F. Giustino, B. D. Malone, C.-H. Park, S. G. Louie, M. L. Cohen, *Comput. Phys. Commun.* **2010**, *181*, 2140.
[61] S. Poncé, E. R. Margine, C. Verdi, F. Giustino, *Comput. Phys. Commun.* **2016**, *209*, 116.